

Intrinsic Capacitance of Molybdenum Disulfide

Jialu Chen, Wesley R. Walker, Luzhu Xu, Olga Krysiak, Zimin She, and Michael A. Pope*



Cite This: *ACS Nano* 2020, 14, 5636–5648



Read Online

ACCESS |

Metrics & More

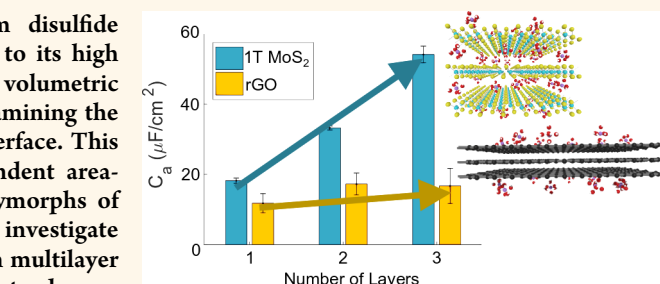
Article Recommendations

Supporting Information

ABSTRACT: The metallic, 1T polymorph of molybdenum disulfide (MoS_2) is promising for next-generation supercapacitors due to its high theoretical surface area and density which lead to high volumetric capacitance. Despite this, there are few fundamental works examining the double-layer charging mechanisms at the MoS_2 /electrolyte interface. This study examines the potential-dependent and frequency-dependent area-specific double-layer capacitance (C_a) of the 1T and 2H polymorphs of MoS_2 in aqueous and organic electrolytes. Furthermore, we investigate restacking effects and possible intercalation-like mechanisms in multilayer films. To minimize the uncertainties associated with porous electrodes, we carry out measurements using effectively nonporous monolayers of MoS_2 , and contrast their behavior with reduced graphene oxide deposited layer-by-layer on atomically flat graphite single crystals using a modified, barrier-free Langmuir–Blodgett method. The metallic 1T polymorph of MoS_2 ($C_{a,1T} = 14.9 \mu\text{F}/\text{cm}^2$) is shown to have over 10-fold the capacitance of the semiconducting 2H polymorph ($C_{a,2H} = 1.35 \mu\text{F}/\text{cm}^2$) near the open circuit potential and under negative polarization in aqueous electrolyte. However, under positive polarization the capacitance is significantly reduced and behaves similarly to the 2H polymorph. The capacitance of 1T MoS_2 scales with layer number, even at high frequency, suggesting easy and rapid ion penetration between the restacked sheets. This model system allows us to determine capacitance limits for MoS_2 and suggest strategies to increase the energy density of devices made from this promising material.

KEYWORDS: molybdenum disulfide, supercapacitors, two-dimensional materials, double-layer capacitance, restacking, intrinsic capacitance

Two-dimensional (2D) materials such as graphene or molybdenum disulfide (MoS_2) are compelling for use in next-generation energy storage devices such as supercapacitors due to their potentially high ion-accessible surface areas, high conductivities, and large electrochemical stability windows.^{1–3} Since an electrode's capacitance is proportional to its specific ion-accessible surface area,⁴ graphene remains one of the most promising electrode materials with $2630 \text{ m}^2/\text{g}$ of potential surface area available for double-layer charging if each side of every sheet were accessible to the electrolyte ions in a thick, dense electrode.⁵ However, since graphene-based materials are known to restack during processing, only a small fraction of this surface area remains accessible. On the other hand, MoS_2 has a lower surface area ($636 \text{ m}^2/\text{g}$),⁶ but this is offset by a considerably higher density ($5.06 \text{ g}/\text{cm}^3$ vs $2.24 \text{ g}/\text{cm}^3$ for graphite), which leads to a potentially higher volumetric capacitance. The field was propelled forward by the discovery that ions could penetrate densely restacked MoS_2 structures resulting in some of the highest reported volumetric capacitances and energy densities of any material, even operating in high voltage-



capable organic and ionic liquid-based electrolytes.⁷ Consequentially, MoS_2 has been increasingly studied in supercapacitor research during the past few years.^{1,2}

Molybdenum disulfide (MoS_2) is a layered transition-metal dichalcogenide, which is typically found in nature as the semiconducting 2H phase, with trigonal prismatic coordination structure.⁸ However, upon intercalation with alkali metals such as Li, the metastable 1T phase is obtained.⁹ This intercalation compound is exfoliated into single layers by adding it to water or other polar solvents, which provides the basis for a process called chemical exfoliation¹⁰ that is widely used to generate mixed 1T/2H MoS_2 single layers that can be converted back to 2H through various thermal^{7,10} or solvothermal methods.¹¹ 1T MoS_2 is metallic, with octahedral coordination structure, and is

Received: December 28, 2019

Accepted: April 21, 2020

Published: April 21, 2020



ACS Publications

© 2020 American Chemical Society

5636

<https://dx.doi.org/10.1021/acsnano.9b10182>
ACS Nano 2020, 14, 5636–5648

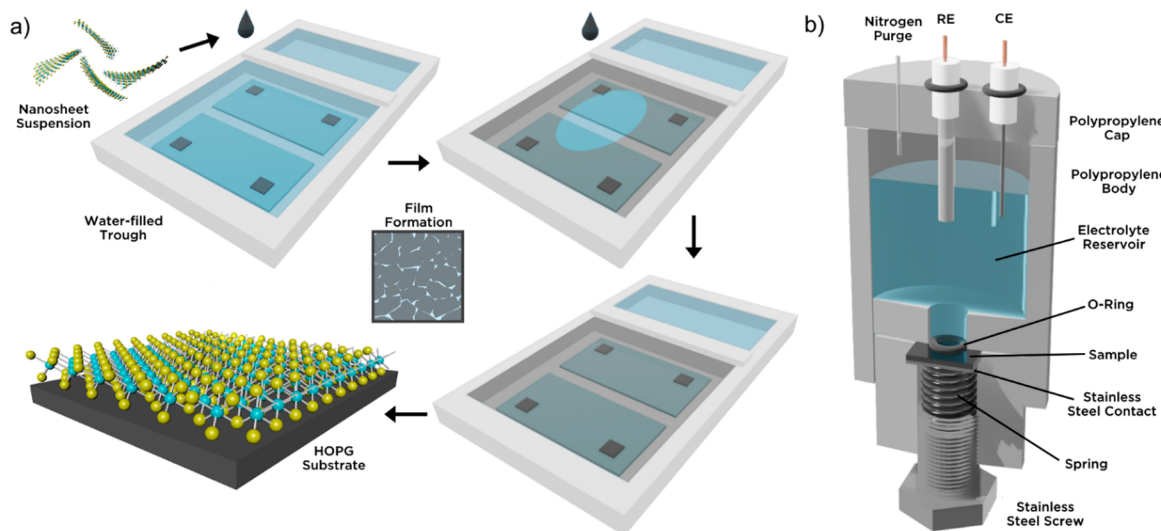


Figure 1. (a) Illustration of modified Langmuir–Blodgett deposition method and (b) diagram of electrochemical cell.

10^7 times more conductive than 2H MoS₂, which makes it a more compelling choice for use in supercapacitors.⁷ Acerce *et al.*¹² demonstrated that dense laminates of chemically exfoliated MoS₂ (1T-rich ~70%) as electrodes for supercapacitors and their ultrahigh volumetric capacitance of ~400 to ~650 F/cm³, which approach those of high performing MXenes, which in contrast, have a limited electrochemical stability window.¹

Subsequently, 1T-rich MoS₂ has been fabricated in various morphologies, ranging from flower-like^{13–16} to spherical^{17–19} to foam-like and continue to demonstrate impressive performance.^{20,21} While supercapacitor research incorporating MoS₂ has been plentiful, fundamental studies of the material are lacking. We are especially interested in the charge storage behavior of MoS₂ when it comes to restacking. Previously, it was shown that increasing graphene layers does not result in increased capacitance due to the way that the layers restack.²² MoS₂ is thought to avoid such pitfalls through easier ion intercalation between the restacked layers.⁷ Furthermore, unlike graphene^{23–27} and graphite,^{28–30} there have been no reports of the intrinsic double-layer capacitance (C_a in $\mu\text{F}/\text{cm}^2$) of the MoS₂/electrolyte interface (1T or 2H, single layer or bulk). This may be due, in part, to the unavailability of large enough single crystals of MoS₂ to be tested in an electrochemical cell, in contrast to highly oriented pyrolytic graphite (HOPG) which can be obtained in ~cm² sizes that allowed for extensive electrochemical measurements on graphite's edge and basal planes to be carried out since the 1970s.^{28,29}

C_a is an important metric that allows for more direct comparison between the charge storage capabilities of different supercapacitor electrode materials. However, the previously mentioned thick-film electrodes are ill-suited for this purpose because of their porosity. In a porous system, C_a measurement requires estimations of accessible surface area, but it is not well understood which pores contribute to double-layer charging.²³ Furthermore, C_a can be affected by the electrode morphology.^{29,31} To circumvent these challenges, fundamental studies of double-layer charging, when possible, should be carried out on flat electrodes with little to no porosity or surface roughness.^{23,27}

The intrinsic capacitance of graphite and of graphene has been well-studied.^{23–27,30,32} The early studies by Randin and

Yeager on HOPG revealed an anomalously low capacitance of the basal-plane of graphite ($3–4 \mu\text{F}/\text{cm}^2$).^{28,29} It was theorized that the double-layer capacitance was not dominated by the Helmholtz layer capacitance (C_H) of the electrolyte, as was known to be the case for a metal,³³ but dominated by a space charge capacitance (C_{SC}) within the electrode itself. This was commonly observed for semiconductor electrodes and was later, and more correctly, attributed to a low density of electronic states near the Fermi energy for graphite which is a semi-metal.²⁷ Since C_H is usually considerably larger than C_{SC} , C_a can often be approximated as C_{SC} . In pristine graphene, this effect manifests as what is termed a low quantum capacitance (C_Q) that has also been measured to be $3–4 \mu\text{F}/\text{cm}^2$, behaving almost identically to HOPG, for graphene obtained by mechanical exfoliation²⁴ or chemical vapor deposition.²⁶ Our work^{23,27} and others^{34,35} have shown that defects and functional groups can act to boost C_Q of graphene-based materials enabling them to act more like glassy carbon, a metallic form of carbon compared to graphene. Only then is it possible to achieve the often reported theoretical capacitance of 400–500 F/g, if all (defective) graphene surface area was exposed to the electrolyte ($\sim 15–20 \mu\text{F}/\text{cm}^2 \times 2630 \text{ m}^2/\text{g}$).²³

Since 1T MoS₂ is also a semi-metal, its intrinsic capacitance may also be limited by electronic properties rather than by the electrolyte. Furthermore, the relatively large bandgap of 2H MoS₂ (~1.9 eV for a single layer) makes it almost insulating, and thus we expect its C_a to be low and dominated by the space charge capacitance effects known for commonly investigated bulk semiconductors such as silicon and germanium. In order to identify the theoretical limits of MoS₂-based supercapacitors and to provide insight into charging mechanisms in this technologically important material, it is of paramount importance to study these intrinsic material properties.

In this study, we attempt to probe C_a of chemically exfoliated, monolayer MoS₂ in both the 2H and 1T phases. To do so, we employ a modified Langmuir–Blodgett technique,⁶ as shown in Figure 1a, to coat atomically flat HOPG surfaces with MoS₂ monolayers in order to probe their differential capacitance behavior by impedance spectroscopy as a function of frequency and DC voltage. The resulting films were characterized in a spring loaded electrochemical cell, as

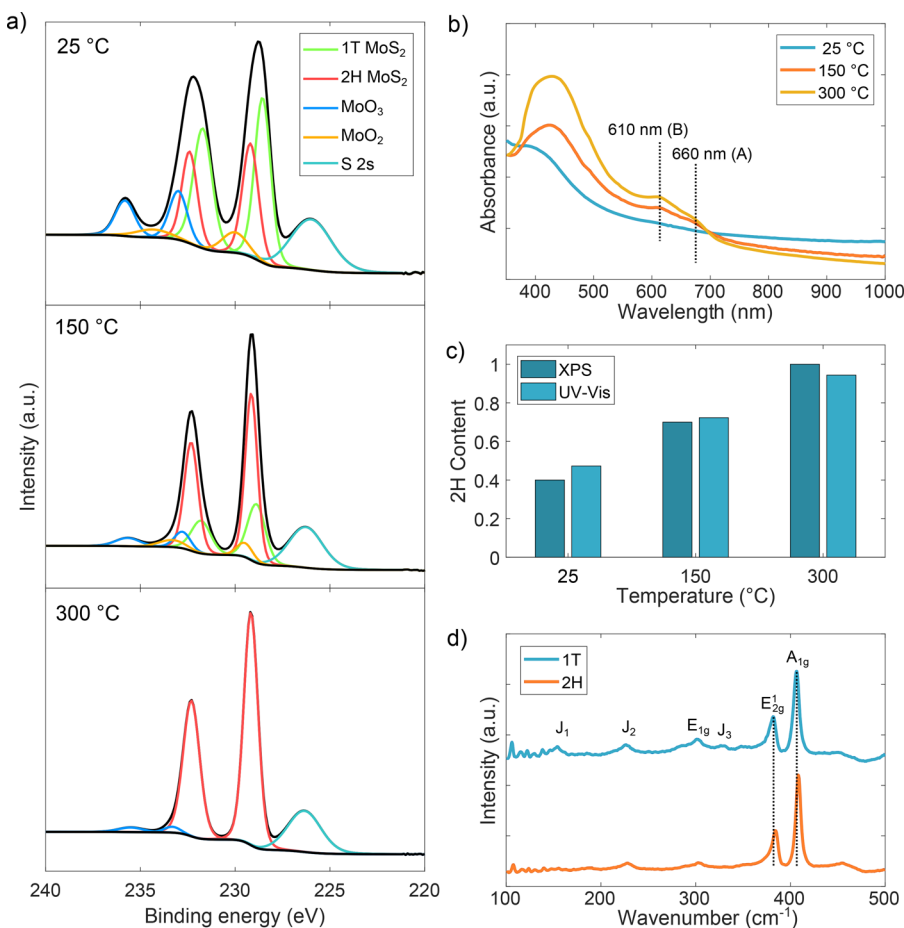


Figure 2. (a) XPS spectra (black) of MoS₂ following heat treatment at various temperatures and corresponding fitted curves for 1T MoS₂ (green), 2H MoS₂ (red), S 2s (teal), MoO₃ (blue), and MoO₂ (orange). (b) UV–vis absorption spectra of MoS₂ dispersion. (c) Comparison of 2H content calculated by XPS and UV–vis data. (d) Raman spectra of the MoS₂ before (blue) and after (red) heat treatment at 300 °C.

shown in Figure 1b, to determine surface coverage, surface roughness, layer number, and chemistry/phase. Using layer-by-layer deposition, single-, double-, and triple-layer MoS₂ and reduced graphene oxide (rGO) electrodes are also investigated to probe restacking effects. The results are used to estimate the theoretical limits for gravimetric and volumetric capacitance and recommendations will be made on how to increase this limit.

RESULTS AND DISCUSSION

Characterization of Exfoliated Materials. Figure 2a shows the X-ray photoelectron spectroscopy (XPS) spectra of the Mo 3d state for samples before and after heat treatment at 150 and 300 °C, as well as deconvolution of the spectra obtained by curve fitting. Papageropoulas and Jaergerman reported the sensitivity of XPS to the differences in the Fermi levels between 1T and 2H MoS₂.³⁶ Following heat treatment, the contribution of 1T MoS₂ (green) to the binding energy of Mo⁴⁺3d_{5/2} and Mo⁴⁺3d_{3/2} is almost entirely diminished, shifting peak positions lower by ~0.7 eV with restoration of the 2H MoS₂ phase (red). By calculating the area under the 1T and 2H MoS₂ peaks, we can obtain the phase composition for each type of sample. For untreated samples, the 2H content was 39.8%, and the 1T content was 60.2%, while the 2H and 1T content of samples treated at 150 °C was 70.7% and 29.3%, respectively, and the 2H content of samples treated at 300 °C was 100%. This is in good agreement with results previously

reported by Eda *et al.*¹⁰ A complete breakdown of the sample composition as determined by XPS can be found in the Supporting Information (Table S1).

The XPS results also indicate the presence of MoO₂ and MoO₃ which comprise 5.72% of the bulk MoS₂ powder but are also formed during processing when the material is exposed to light and oxygen *via* a mechanism recently reported by us.³⁷ The untreated samples showed 22.4% MoO_x content, which was reduced to 17.1% MoO_x content following heat treatment at 150 °C and further reduced to 3.61% MoO_x content at 300 °C. Acid flocculation was suspected to have caused the increase in MoO_x content, which was verified through XPS of MoS₂ nanosheets before and after acid treatment and can be found in the Supporting Information (Figure S3). While there was a difference in the MoO_x content of the MoS₂ nanosheets, there was no clear change in the electrochemical properties (Figure S3).

These results were validated by UV–vis measurements of the MoS₂ dispersion, shown in Figure 2b, which are in agreement with previously reported results.⁶ The peak observed between 350 and 450 nm indicates a direct excitonic transition from the valence to the conduction band and is enhanced upon transforming 1T MoS₂ to the 2H polymorph through heat treatment.³⁸ Similarly, the peaks observed at ~610 nm and ~660 nm correspond to B1 and A1 direct excitonic transitions in 2H MoS₂, respectively. The peaks at ~610 and ~660 nm were only observed in the 2H MoS₂

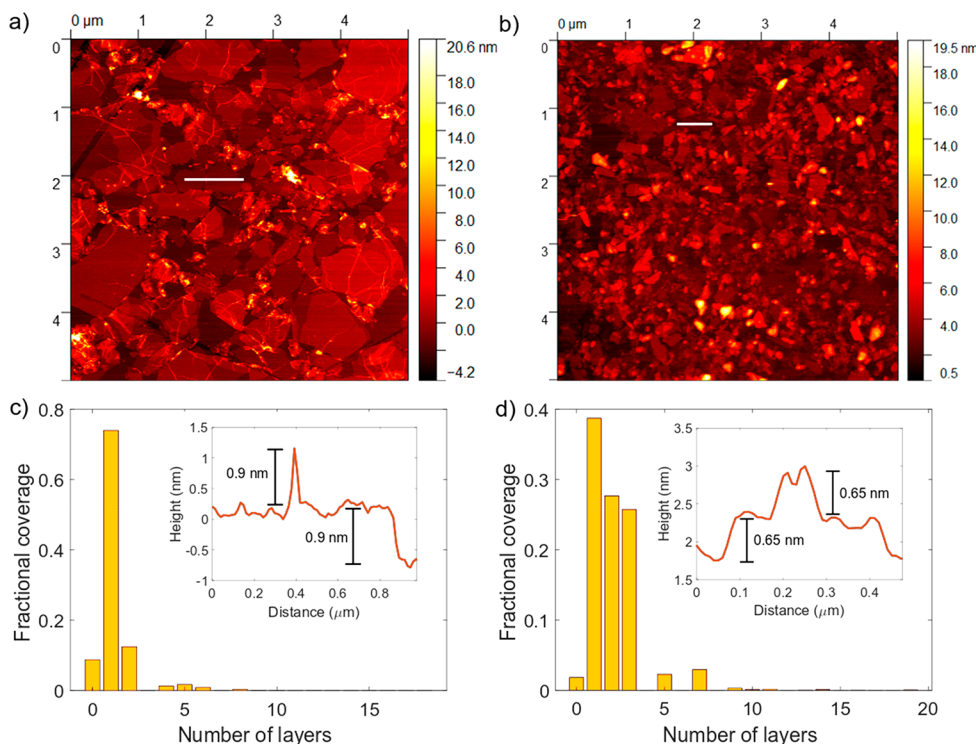


Figure 3. AFM images of (a) rGO and (b) MoS₂ films on HOPG substrates and height distribution of these (c) rGO and (d) MoS₂ films. Height profiles from the AFM images are shown in the inset of the height distribution plots.

sample. As shown in Figure 2c, for untreated samples, the 2H content was estimated from the UV-vis data using the empirical relation suggested by Knirsch *et al.*³⁹ as 47.3%, while the 2H content of samples treated at 150 °C was 72.3% and the 2H content of samples treated at 300 °C was 94.4%. This estimate is in good agreement with the XPS results and further validates the accuracy of this relationship using much easier to obtain UV-vis data. For brevity, in the rest of the manuscript, we refer to the untreated samples and samples treated at 300 °C as “1T MoS₂” and “2H MoS₂”, respectively; however, they are more accurately “1T-rich” and “2H-rich” samples.

Raman spectroscopy results are shown in Figure 2d and were used to confirm 1T to 2H phase transition following heat treatment. Peaks can be observed at $\sim 382\text{ cm}^{-1}$ (E_{2g}^1) and $\sim 407\text{ cm}^{-1}$ (A_g^1) for both samples, which are vibrational modes, associated respectively with in-plane and out-of-plane vibrations of 2H MoS₂.⁶ The broadening and shifting of these peaks to lower wave numbers after exfoliation are typical of the 1T phase.⁴⁰ In the 1T MoS₂ sample, there are also three characteristic peaks observed at 154 cm^{-1} , 226.1 cm^{-1} , and 326.4 cm^{-1} , also known as the J_1 , J_2 , and J_3 peaks. These peaks, indicative of 1T MoS₂, are significantly diminished following heat treatment, suggesting transformation into the 2H phase.⁶

Characterization of Langmuir Films and Coated Substrates. Figure 3a,b illustrates typical AFM images of the Langmuir films coated onto HOPG. The films are composed of densely tiled flakes. In the case of rGO (Figure 3a), the thickness of a monolayer is approximately 0.7–1.0 nm, which is in good agreement with the typical thickness observed for single-layer rGO.⁵ Likewise, a double layer was found to be 1.8 nm thick. The surface roughness was calculated to be 1.01 ± 0.002 and did not vary significantly between layer number or material. rGO films showed wrinkled flakes with diameters on the order of microns, as seen in Figure 3a. As mentioned in the

Experimental Methods, a Python script was used to fit a sum of Gaussians to the raw height data, resulting in a calculation for fractional coverage by layer number. An illustration of how the script fits Gaussian functions to the height distribution can be seen in the Supporting Information (Figure S4). In the rGO sample, 92.2% surface coverage was obtained, with 74.0% of the surface covered by monolayers and 18.2% covered by two or more layers.

The MoS₂ films displayed a less wrinkled morphology, and the sheet sizes were often smaller than 1 μm in diameter, as shown in Figure 3b. For MoS₂, the thickness of a monolayer is approximately 0.65 nm, which is demonstrated by the thickness profile of a single nanosheet.⁴¹ Similarly, a double layer was found to be 1.3 nm thick. In this sample, 97.7% surface coverage was obtained, with 38.7% coverage by monolayers, 27.7% coverage by bilayers, and 31.3% coverage by three or more layers. Despite a generally uniform coating, the MoS₂ films were occasionally interrupted with flakes up to 25 nm thick. These aggregates were likely caused by incomplete intercalation of bulk MoS₂ since they are orders of magnitude larger than 0.65 nm, the expected thickness of single-layer MoS₂.⁴¹ Since lithium was unable to intercalate these thicker flakes, it is reasonable to assume that the electrolytes used were unable to do so as well. Therefore, the presence of the thicker flakes should not contribute considerably to the areal capacitance of the electrode. This assumption will be further validated in the electrochemical results discussion below.

SEM images shown in Figure 4 demonstrate the film coverage over larger areas. ImageJ was employed to determine the fractional coverage of the films through pixel counting, as detailed in the Supporting Information (Figure S5). rGO films possessed an average fractional coverage of $87.9 \pm 3.5\%$. Conversely, MoS₂ films had an average coverage of $92.1 \pm$

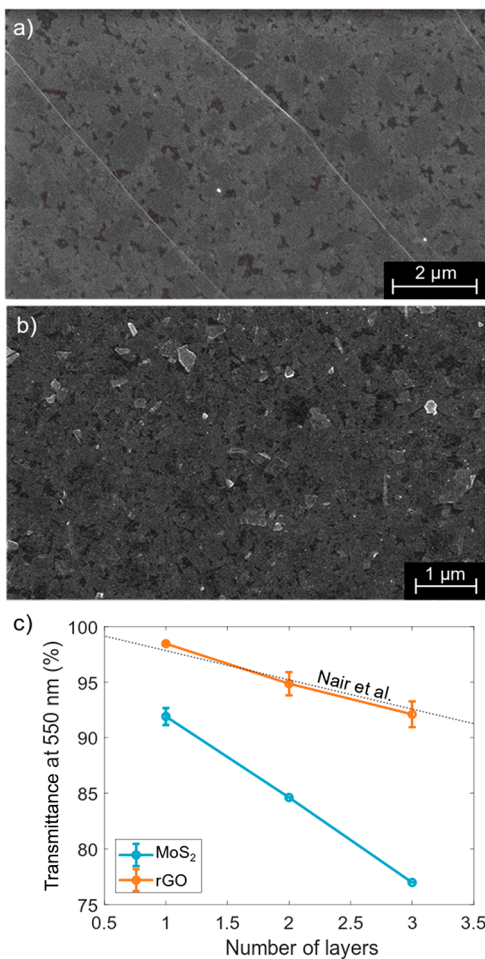


Figure 4. SEM images of (a) rGO and (b) MoS₂ films on HOPG substrates and (c) transmittance at 550 nm of MoS₂ and rGO films as a function of coating layers.

1.6%, which was in agreement with the values obtained from AFM image analysis. This is evident in Figure 4, which shows denser tiling for the rGO film compared to the MoS₂ film. As the number of layers increased, MoS₂ film coverage jumped to 100% for double- and triple-layer films, as the underlying substrate could no longer be identified.

Since it was not possible to probe the thickness of bilayer and trilayer films accurately by AFM due to the lack of exposed substrate, we relied on UV-vis to confirm the thickness scaled linearly with layer number. Glass substrates were coated with monolayer, bilayer, and trilayer Langmuir films of both materials, and their transmittance was measured. As shown in Figure 4c, a monolayer rGO film exhibited a transmittance of 97.6% at 550 nm, when corrected with film coverage, decreasing by 2.1–2.8% with every further deposition. This is in good agreement with the theory and results presented by Nair *et al.*, which showed that a graphene monolayer absorbs 2.3% of white light.⁴² Conversely, a single-layer MoS₂ film exhibited a transmittance of 92%, decreasing by 7–8% with every further deposition. This is comparable to previously reported values, which claimed 90% transmittance for single-layer MoS₂, decreasing by 8–10% per added layer.⁶ Further details regarding the Langmuir films produced, including transfer efficiency, can be found in the Supporting Information (Figure S6).

Electrochemical Analysis of Monolayer Electrodes. Cyclic voltammograms (CVs) obtained for pure HOPG were rectangular in nature from voltages of −0.5 to 0.5 V at 100 mV/s, as seen in Figure S7 of the Supporting Information, with a small enhancement of cathodic current below about −0.3 V likely generated by the reduction of residual oxygen in the cell. This oxygen reduction was found to cause a significant and irreversible increase in capacitance over the entire potential window likely caused by the reactive oxygen species generated (for example, H₂O₂). The reactive oxygen species would then interact with the MoS₂, forming either soluble molybdates and high activity edge sites or possibly pseudocapacitive MoO₃.³⁷ Because of this, a voltage window of −0.3 to 0.5 V was used to avoid damaging the films.

As shown in Figure 5, EIS was used to investigate the capacitance of all films as a function of frequency and DC potential. The lines in the plot represent average values of three or more runs, while the shaded regions represent the ± standard deviation of the measurement. The inset of Figure 5a,b shows that the capacitance of the bare HOPG ranging from 1.5 to 2 μF/cm² between −0.3 and 0.5 V. This is only slightly lower than the 2 to 3 μF/cm² reported in literature, but the capacitance of HOPG is known to be influenced by quality of the crystal and number/density of edge-planes exposed.^{23,28,29} The capacitance was fairly constant with frequency, showing <19.2% change between 10 and 1000 Hz. The voltage dependence curve in the inset of Figure 5b demonstrates a rounded V shape with a minimum around −0.1 V *vs* Ag/AgCl (1 M) which coincided with the open circuit voltage (OCV). This is similar to what has been reported by Randin and Yeager in their pioneering studies.^{28,29} For the MoS₂, in the 1T films in particular, below about 10 Hz, the slope of the capacitance–frequency curves typically increased significantly due to slower Faradaic charging processes. Thus, 100 Hz was chosen for comparing between films, as this frequency is also sufficiently far away from the knee frequency dictated by the RC time constant of the cell.⁴³ Depending on the film capacitance and the position of the reference electrode (which we attempted to keep the same for each measurement), the knee frequency ranged from 10⁴ to 10⁵ Hz.

The most obvious difference in the frequency dependence curves is the large difference in the magnitude of the capacitance between 1T and 2H MoS₂. As shown in Figure 5b, this considerable difference in capacitance exists only at potentials more negative than the OCV until the capacitance of the 1T MoS₂ drops significantly after reaching 0.1 V and continues to decrease past that point, while 2H MoS₂ shows comparatively little voltage dependence. The large difference observed under negative polarization might be expected due to the metallic *vs* semiconducting nature of the two materials.⁷ However, the complex voltage dependence of the 1T MoS₂ material is surprising and not readily explained. For example, we might consider these changes a result of changes to the Stern layer (adsorbed ions or adsorbed solvated ions that make up the inner *vs* outer Helmholtz planes) at either side of the point of zero charge (pzc) or potential-dependent pseudocapacitance (*i.e.*, intercalation, redox active function groups) or possibly potential-dependent electronic effects within the material itself.

If we first consider the Stern model, under positive polarization, the fluorine anions are expected to form the outer Helmholtz plane, resulting in an accumulation of fluorine anions near the electrode surface.⁴⁴ The higher polarizability of

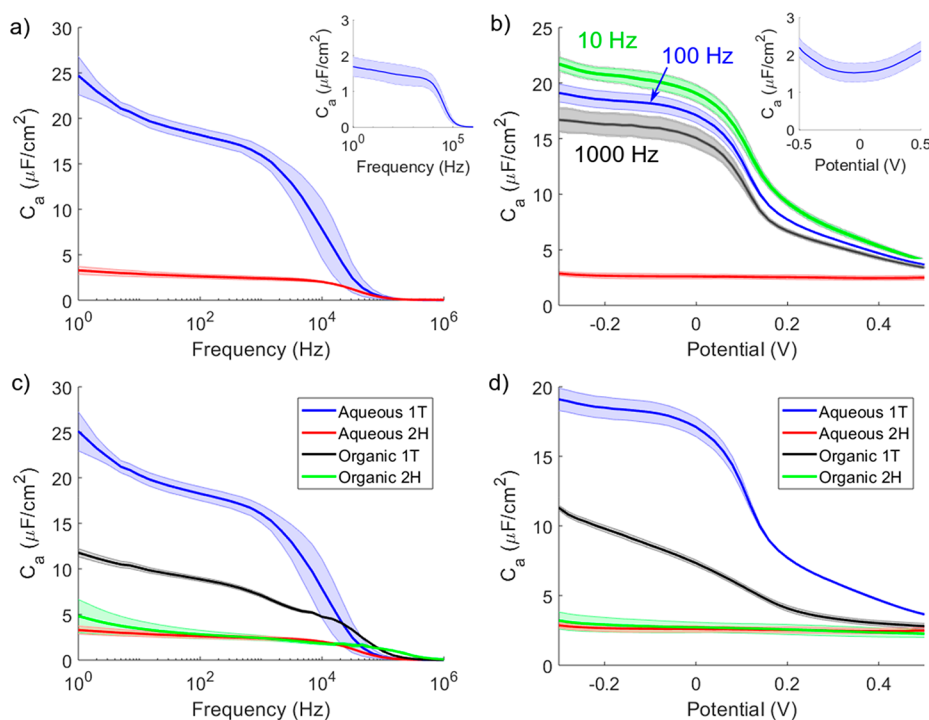


Figure 5. Areal capacitance of 1T (blue) and 2H (red) MoS_2 films in aqueous electrolyte as a function of (a) frequency at -0.14 V vs Ag/AgCl (1 M) and (b) potential at 100 Hz for 2H MoS_2 and at various frequencies for 1T MoS_2 , with corresponding measurements on bare HOPG in the inset. Comparison between areal capacitance of 1T and 2H MoS_2 films in aqueous and organic electrolyte as a function of (c) frequency at -0.14 V vs Ag/AgCl (1 M) and (d) potential at 100 Hz.

anions often leads to the shedding of their solvation shell and specific adsorption which enhances the capacitance under positive polarization. However, fluoride is not a typical anion and is not very polarizable because it is small. Consequently, it is typically solvated in polar solvents.⁴⁵ Similarly, sodium cations are expected to accumulate near the electrode surface when negatively polarized. Cations typically have a stronger solvation shell and do not specifically adsorb. However, if electro-adsorbed, their smaller size can lead to higher capacitance, due to smaller distance of closest approach.^{44,46} The residual negative charge of the MoS_2 without any applied bias, due to the chemical reduction of MoS_2 with *n*-butyllithium, may be capable of stripping the solvation shell and allowing electro-adsorption.

The ratio of the radius of a solvated fluoride ion (0.358 nm)⁴⁷ to the radius of an unsolvated sodium ion (0.102 nm)⁴⁸ is 3.51, whereas the drop in capacitance ratio observed is between 2.4 and 4.5 depending on the value of the capacitance chosen in the sloping positive polarization branch of the potential dependence. Thus, the ratio fits, however, the low capacitance under positive polarization is much smaller than $\sim 16\text{--}25 \mu\text{F}/\text{cm}^2$, the capacitance value typically reported for the Helmholtz layer measured in classic experiments on mercury in aqueous NaF.

Faradaic reactions may also contribute to the observed potential dependence of 1T MoS_2 resulting in what is known as pseudocapacitance. Such reactions are often a strong function of frequency, and thus one might expect the shape of the capacitance–potential plot to change with the frequency plotted.²³ The presence of oxygen during MoS_2 synthesis can result in defects that enhance capacitance in aqueous electrolytes, which are then suppressed in organic electrolytes.^{49,50} Furthermore, the multiple oxidation states of Mo

allow for faradaic charge storage in aqueous electrolytes.⁵⁰ As shown in Figure 5b, the shape remains the same, irrespective of frequency. The magnitude of the capacitance is simply diminished with increasing frequency. Furthermore, upon analyzing the frequency dispersion (Figure S8 of the Supporting Information), there appears to be no change between 1T and 2H MoS_2 in the range of 10–100 Hz, which suggests the absence of slower pseudocapacitive reactions.

The MoS_2 electrodes were also tested in an organic electrolyte in an attempt to eliminate the effect that proton transfer reactions between surface functional groups which might be present on the MoS_2 (for example, the MoO_x defects detected by XPS) and the aqueous electrolyte would have on the capacitance. Figure 5c demonstrates that switching to an organic electrolyte caused the capacitance to drop by nearly a factor of 2. Upon inspecting the entire frequency range (Figure S9 of the Supporting Information), the ratio is approximately 2 until a frequency of 10^4 Hz is reached, at which the measured capacitance in aqueous electrolyte is much smaller. This rapid decrease in the ratio can be attributed to differences in the RC time constant, which dictate when the plateau in the frequency dependence ends. Moreover, at the lower frequencies where Faradaic reactions can occur, the capacitance ratio is relatively constant, suggesting that pseudocapacitance from slower redox reactions is not the cause of the capacitance drop.

As shown in Figure 5d, the change in electrolyte similarly results in a drop by approximately 2 over the entire potential range, with a higher ratio for potentials near 0 V and a lower ratio for more positive or negative potential values (Figure S9 of the Supporting Information). The fact that a similar drop in capacitance was observed over all voltages suggests the high capacitance observed for 1T MoS_2 under negative polarization is not due to redox reactions involving proton transfer. The

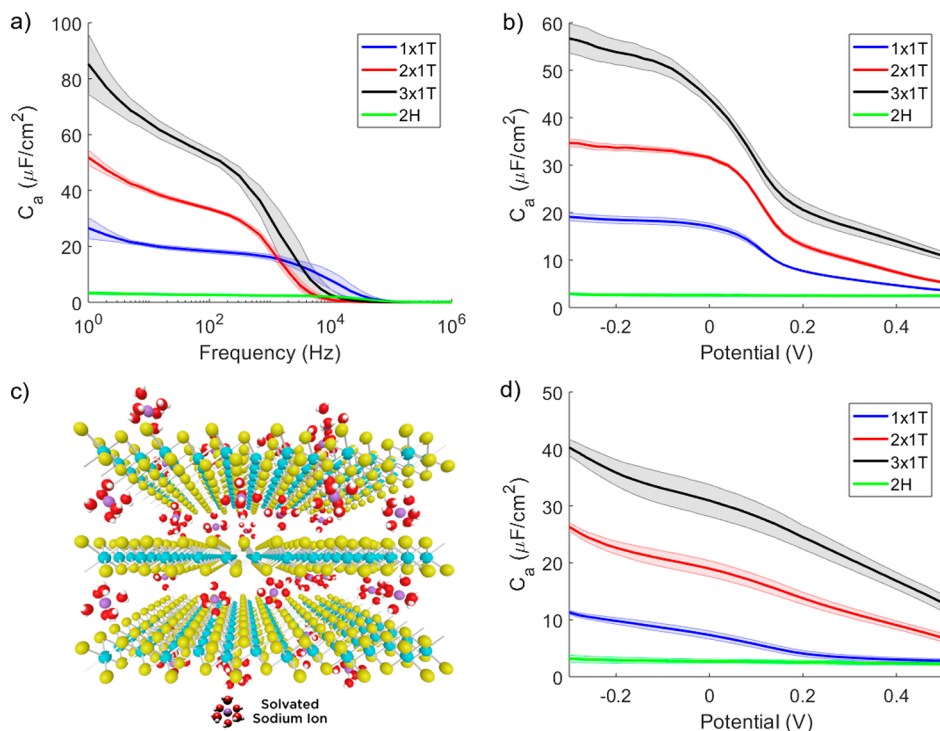


Figure 6. Areal capacitance of multilayer MoS₂ films in aqueous electrolyte as a function of (a) frequency at -0.14 V vs Ag/AgCl (1 M) and (b) potential at 100 Hz. (c) A schematic diagram of the restacking behavior of MoS₂. (d) Areal capacitance of multilayer MoS₂ films in organic electrolyte as a function of potential at 100 Hz.

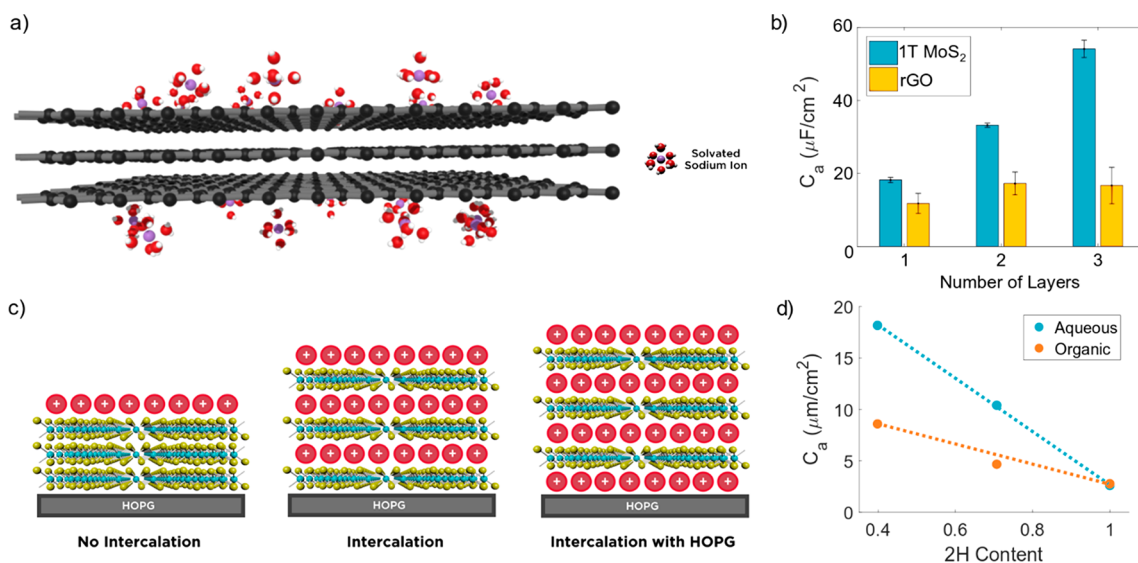


Figure 7. (a) Schematic diagram of the restacking behavior of rGO. (b) Areal capacitance plotted against number of layers for both 1T MoS₂ and rGO multilayer electrodes. (c) A schematic diagram illustrating the various possible charging mechanisms. (d) Measured areal capacitance at 100 Hz and -0.14 V vs Ag/AgCl (1 M) plotted against 2H content.

reduction in capacitance in organic electrolyte compared to aqueous electrolyte can be explained partially by the Stern theory. The radius of a solvated tetraethylammonium ion is 0.482 nm, while the radius of an unsolvated tetraethylammonium ion is 0.4 nm.⁵¹ The ratio of unsolvated aqueous cationic radius to unsolvated organic cation radius is 4, which is over two times higher than the ratio of measured capacitances at more negative polarizations where the solvation shell is expected to be stripped. Meanwhile, the ratio of solvated aqueous cationic radius to solvated organic cation radius is

1.35, which almost exactly matches the ratio of measured capacitances at more positive polarizations where the solvation shell is expected to be intact. This strongly suggests that the differences in ion size are the reason behind the drop in capacitance upon changing electrolytes.

In order to investigate intercalation effects, the same methods were applied to multilayer MoS₂ electrodes fabricated layer-by-layer using the same monolayer MoS₂. Figure 6a shows the frequency dependence of multilayer MoS₂ films. At low frequencies, the capacitance is found to increase linearly

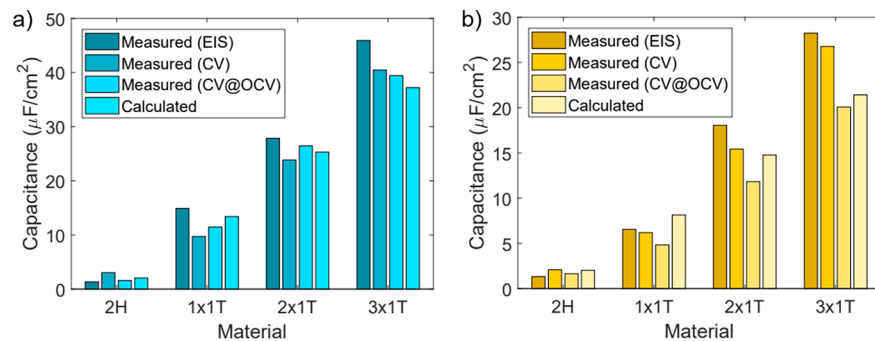


Figure 8. Comparison between measured and calculated values of areal capacitance for MoS_2 monolayer electrodes in (a) aqueous and (b) organic electrolyte.

with layer number, suggesting that ions can access the interlayer galleries between restacked MoS_2 . The slope of the low-frequency portion of the curve (*i.e.*, the frequency dispersion) increases slightly with each layer, indicating that charging the underlying layers takes place over a longer time scale. Figure S7a,c shows normalized frequency dependence plots which better show this increased frequency dispersion.

Figure 6b demonstrates the voltage dependence of the multilayer MoS_2 films obtained at 100 Hz. The capacitance of the films increases almost linearly with layers over nearly the entire potential range. This suggests that ions can intercalate between restacked sheets, as demonstrated previously,¹² and also that this is independent of potential, unlike more typical intercalation reactions which occur at some defined redox potential. Figure 6c illustrates how the restacking of MoS_2 still allows for ion intercalation between the nanosheets, resulting in layer-dependent capacitance behavior.

Additionally, the capacitance of multilayer MoS_2 was investigated in organic electrolyte, as shown in Figure 6d. The general patterns observed in organic electrolyte were also observed upon addition of multilayers. When it comes to double- and triple-layer films, the continuous increase in capacitance suggests that the organic electrolyte is still able to intercalate the MoS_2 layers. Therefore, the decrease in capacitance of a MoS_2 monolayer observed by switching from aqueous to organic electrolyte cannot be attributed to restacking layers. Rather, it is more likely caused by larger ion size. Moreover, this provides evidence for the previously made hypothesis that unexfoliated 2H MoS_2 chunks seen in the AFM images do not contribute to the measured capacitance of the monolayer. Previous studies done on MoS_2 supercapacitors also reported a reduction by half after switching to an organic electrolyte from an aqueous electrolyte.¹²

For comparison, the same experiments were performed for rGO films, as seen in the Supporting Information (Figure S10). The capacitive behavior of multilayer rGO was investigated to determine the restacking behavior of rGO and compare it to that of 1T MoS_2 . While there is an increase in capacitance between the first and second layer of rGO, it does not add as if the layers were independent of each other. This is because graphene nanosheets aggregate and restack when layered on top of each other, reducing accessible specific surface area and decreasing gravimetric/volumetric capacitance.²² Figure 7a illustrates how the restacking of rGO nanosheets prevents ion intercalation. This is in contrast to the behavior of multilayer MoS_2 electrodes, which show a continuous increase in capacitance with layer number, as shown in Figure 7b.

The measured capacitance of each MoS_2 sample will now be compared to what we might expect from theory for pure phase 1T and 2H MoS_2 based on theory for semi-metals and semiconductors, respectively. The intrinsic capacitance of both materials was calculated and compared with the measured values at the OCV (−0.14 V), which we expect to be approximately the pzc. 2H MoS_2 was treated as a semiconductor, and the space charge capacitance for the pzc was calculated based on the charge carrier concentration (n):

$$C_{\text{SC}} = \left[\frac{2\epsilon\epsilon_0^2 n}{kT} \right]^{0.5}$$
, where ϵ is the relative permittivity of MoS_2 (3.7)⁵² and ϵ_0 is the permittivity of vacuum.^{28,29,53} Previously, a charge carrier concentration of $7.36 \times 10^{16} \text{ cm}^{-3}$ was measured by Lee *et al.* for MoS_2 thin films, and this value was used in our calculations.⁵⁴ This leads to an estimated $C_{\text{SC},2\text{H}} = 0.548 \mu\text{F}/\text{cm}^2$. On the other hand, Gerischer's relationship was used to predict the capacitance of a semi-metallic 1T phase as a function of the DOS (N_0) near the Fermi energy: $C_{\text{SC}} = \sqrt{\epsilon\epsilon_0 N_0 e}$, where e is the charge of an electron.²⁴ The DOS was calculated to be $1.367 \times 10^{22} \text{ eV}^{-1} \text{ cm}^{-3}$, which is in good agreement with the values reported by Wang *et al.*⁵⁵ This leads to an estimated $C_{\text{SC},1\text{T}} = 25.2 \mu\text{F}/\text{cm}^2$.

While ions have been shown to intercalate 1T MoS_2 nanosheets, it is uncertain whether charge is stored solely on the exposed side of the film ("no intercalation") or if ions can penetrate between the film and the substrate which could cause double-layer charging at both the other side of MoS_2 ("intercalation") as well as exposing additional HOPG to the electrolyte ("intercalation with HOPG"). Figure 7c illustrates each case of charging behavior considered. The expected intrinsic capacitance in each of these cases was calculated and compared with measured results. To calculate the intrinsic capacitance (C_a), the space charge capacitance (C_{SC}), Helmholtz capacitance (C_H), and diffuse double-layer capacitance (C_{diff}) were combined according to the work of Gerischer.³⁰ Eq 1 was used, and the Helmholtz capacitance of $25 \mu\text{F}/\text{cm}^2$ was used for aqueous electrolyte⁴ and $11 \mu\text{F}/\text{cm}^2$ for organic electrolyte.⁵⁶

$$\frac{1}{C_a} = \frac{1}{C_{\text{SC}}} + \frac{1}{C_H} + \frac{1}{C_{\text{diff}}} \quad (1)$$

The capacitance of a monolayer MoS_2 electrode with intermediate 2H content was also measured. Capacitance values at the OCV were plotted against measured 2H content, as shown in Figure 7d. These data were used to extrapolate expected capacitance values for "pure phase" 1T and 2H MoS_2 monolayer electrodes. When considering the cases assuming

intercalation, the measured value was divided by 2 to account for the doubling of surface area with both sides exposed. Therefore, the experimental value of pure phase 1T MoS₂ would be reduced from 29.8 to 14.9 $\mu\text{F}/\text{cm}^2$, while it would be reduced from 2.7 to 1.35 $\mu\text{F}/\text{cm}^2$ for 2H MoS₂ in aqueous electrolyte. Figure 8 shows the comparison of values calculated from theory and values taken from EIS and CV measurements.

Figure 8a,b summarizes the comparison between measured and calculated values of the intrinsic capacitance at the OCV under assumptions for the “intercalation with HOPG” case, which provided the best match between values. They compare calculated values for monolayer, double-layer, and triple-layer 1T MoS₂ films against their measured values, for aqueous and organic electrolytes, respectively. Since the capacitance of multilayer electrodes increased substantially with layer number, the case of “no intercalation” was rejected.

Similar to EIS values, the CV capacitances were corrected for 1T/2H phase composition. Figure 8 compares the different measured and calculated values in a bar chart. In general, the measured values from CV were slightly lower than that of EIS for 1T MoS₂ and slightly larger for 2H MoS₂. When it came to measurements in aqueous electrolyte, there were generally higher capacitances calculated for CV@OCV values than for CV values due to the shape of the CV curve being slightly wider at more negative capacitance values. Conversely, for measurements in organic electrolyte, the CV@OCV values were generally lower since the shape of the CV curve was more uniform. Any discrepancy between the EIS values and CV values is caused by the fact that voltage dependence of the EIS curves is much more significant compared to that of the CV curves, resulting in much higher capacitances recorded for negative potentials. Regardless, there is good agreement with EIS values and values calculated from theory.

When comparing the extrapolated pure phase capacitance measurements in both aqueous and organic electrolyte with calculated values assuming intercalation with HOPG contribution, there is good agreement in all cases. Deviations between values can be attributed to either experimental error or the presence of oxygen defects which can increase the capacitance through pseudocapacitive contributions.

The experimental intrinsic capacitance values for monolayer 1T and 2H MoS₂ can be used to calculate theoretical gravimetric and volumetric capacitance limits for supercapacitors made with these materials. When multiplying the obtained $C_{a,1T} = 14.9 \mu\text{F}/\text{cm}^2$ from measurements in aqueous electrolyte with 636 m^2/g , the specific surface area of MoS₂, we arrive at 94 F/g, the theoretical gravimetric capacitance.⁶ By further multiplying the value with 5.06 g/cm³, the density of MoS₂, we arrive at 479 F/cm³, the theoretical volumetric capacitance.⁵⁷ This value falls within the volumetric capacitance range of 400–650 F/cm³ reported by Acerce *et al.* for their 1T MoS₂ nanosheet supercapacitor in aqueous electrolyte.⁷ Furthermore, by using the obtained $C_{a,1T} = 6.55 \mu\text{F}/\text{cm}^2$ from measurements in organic electrolyte, we arrive at theoretical gravimetric and volumetric capacitances of 42 F/g and 211 F/cm³, respectively. The latter value almost perfectly matches the volumetric capacitance Acerce *et al.* reported for measurements in TEABF₄/ACN of 199 F/cm³.⁷ Similar calculations for 2H MoS₂ predict a gravimetric and volumetric capacitance limit of 8 F/g and 42 F/cm³, respectively, in both electrolytes. The performance of 1T MoS₂ supercapacitors appears to be at the theoretical volumetric capacitance limit. Therefore, to further improve capacity, one must consider

introducing other materials,² incorporating defects which enable pseudocapacitance,⁴⁹ or creating asymmetric supercapacitors, in which MoS₂ is used as the negative electrode due to the significantly higher capacitance observed under negative polarization.⁵⁸ Further work is required to determine the reason why the intrinsic capacitance of the 1T polymorph/electrolyte interface approaches that of the 2H polymorph at potentials significantly larger than the pzc.

CONCLUSION

By depositing density tiled monolayers of MoS₂ on HOPG in aqueous and organic electrolytes, we measured the intrinsic capacitance of 1T and 2H MoS₂. The 1T and 2H MoS₂ polymorphs exhibited intrinsic capacitance values of 14.9 $\mu\text{F}/\text{cm}^2$ and 1.39 $\mu\text{F}/\text{cm}^2$, respectively, under negative polarization with little frequency dependence, demonstrating an over 10-fold difference. Over all potentials studied, the capacitance of the electrode/electrolyte interface is reduced when an organic electrolyte is used compared to an aqueous one. This can be explained by a decrease in the Helmholtz capacitance in organic electrolytes. An unexpected result is that the capacitance of the 1T MoS₂/electrolyte interface approaches that of the 2H phase under positive polarization. This suggests that positive polarization causes the 1T polymorph to become electronically similar to the semiconducting 2H polymorph, which is not readily explained and left to future work.

Multilayer MoS₂ was also investigated to explore the effects of restacking. The capacitance of multilayer MoS₂ films increased with each further monolayer deposition, suggesting that MoS₂ nanosheets restack in a way that does not reduce accessible surface area. As a point of comparison, multilayer rGO was also investigated. While there was a slight increase in capacitance between the first and second layers of rGO, there is no further enhancement to the capacitance for subsequent layers. This is because rGO aggregates and restacks when layered on top of each other, reducing accessible surface area and decreasing overall areal capacitance.

The intrinsic capacitance was extrapolated from measured values and also calculated according to previously reported works. In order to determine which assumptions were most likely to be accurate, measured values were compared with the calculated values. Our analysis confirms that electrolyte ions can intercalate between adjacent MoS₂ layers and also between the MoS₂ and HOPG supporting electrode. Using these measured values, we extrapolate theoretical gravimetric and volumetric limits for supercapacitors comprised entirely from 1T MoS₂. The results suggest that these limits have already been reached. As such, introducing defects or other materials or incorporating MoS₂ into the negative electrode of an asymmetric supercapacitor may be necessary to further improve the energy density of MoS₂ based supercapacitors.

EXPERIMENTAL METHODS

Synthesis and Reduction of Graphite Oxide. Graphite oxide (GO) was synthesized using the modified Hummer's method⁵⁹ presented by Marcano *et al.*⁶⁰ 3 g of graphite (Alfa Aesar, 99.9%), 360 mL of H₂SO₄ (Sigma-Aldrich, 95–98%), and 40 mL of H₃PO₄ (Sigma-Aldrich, extra pure, 85% solution in water) were combined. 18 g of KMnO₄ (Sigma-Aldrich) was added as the temperature of the water bath was raised to 40 °C. The mixture was set to stir for 20 h. After cooling to room temperature, 3 mL of 30% H₂O₂ (Sigma-Aldrich) was added to the mixture dropwise, after which the color changed from a dark brown to a light yellow. The obtained slurry was transferred into a centrifuge tube in order to separate the residual

acids and salts from the GO. Centrifugation was carried out at 3500 rpm for 1 h using a Thermo Scientific Central CL2 centrifuge and suspended in water. This process was repeated once by resuspending the pellet in 30% HCl (Sigma-Aldrich), followed by three cycles with ethanol (Fisher Scientific). In the end, the resulting GO suspension was stored in ethanol.

The GO nanosheets were reduced chemically with hydrazine (Sigma-Aldrich, 35 wt % in water) using a modified version of Park's method.⁶¹ A 5 mg/mL as-prepared GO suspension in ethanol was bath sonicated for 5 min. Then, 2 mL of the GO suspension was diluted with 18 mL of dimethylformamide (DMF) (Sigma-Aldrich, ≥99.8%), which has been shown to produce the most stable rGO nanosheet dispersions, in a 20 mL scintillation vial.⁶¹ After the reaction chamber was heated to 140 °C and while stirring at 500 rpm, 80 μL of hydrazine solution was added to the reaction chamber. The mixture was set to stir for 16 h. After the reaction was complete, the dispersion was used immediately as obtained for film deposition to minimize the chance of agglomeration.

Exfoliation of Molybdenum Disulfide. Bulk molybdenum disulfide was exfoliated chemically with *n*-butyllithium using a modified version of Eda's method.⁶ 0.5 g of MoS₂ powder (Sigma-Aldrich, ~6 μm) was mixed with 7 mL of 1.6 M *n*-butyllithium solution in hexane (Sigma-Aldrich) in a 25 mL reaction vessel. After stirring continuously for 3 days in an Ar-filled glovebox (O₂ and H₂O < 1 ppm), the intercalated MoS₂ was collected by filtration into a large beaker, washed with 80 mL of hexane, and diluted with 150 mL of deionized water. Then, the beaker was bath sonicated (TruSonik, 2.5 L, 120 W) for 1 h to complete the exfoliation process. Following sonication, the dispersion was solvent exchanged into DMF.⁶ HCl solution was used to adjust the pH of the dispersion to 2, flocculating the MoS₂. The aggregates of MoS₂ were collected by filtration using Whatman 42 filter paper, then transferred into a centrifuge tube and redispersed in DMF by bath sonication. Finally, the MoS₂ in DMF was centrifuged at 3500 rpm for 1 h to remove unexfoliated MoS₂ using a Fisher Scientific AccuSpin 3.

Characterization. The C/O ratio of the reduced GO (rGO) nanosheets was estimated by energy-dispersive X-ray spectroscopy (EDS) on powders created by drying dispersions in a vacuum oven at 110 °C and found to be ~5.2. As discussed in the Supporting Information (Figures S1 and S2), a study was carried out to maximize the reduction of GO without causing agglomeration of the dispersion, in which the reaction temperature and hydrazine content were varied. This study demonstrated that GO reduction carried out at higher temperatures and with greater hydrazine content showed greater stability. rGO nanosheets that were more completely reduced and therefore more hydrophobic allowed for better dispersion in DCE. This reduced aggregation in the nanosheet solutions, which produced higher quality Langmuir films.

X-ray photoelectron spectroscopy (XPS) was performed on MoS₂ samples with a Thermo-VG Scientific ESCALab 250 X-ray Photoelectron Spectrometer Microprobe, using a monochromatic Al Kα X-ray source (1486.6 eV). Samples were prepared by drop casting aqueous MoS₂ nanosheet suspensions onto Si wafers, followed by drying in a vacuum oven without heat. CasaXPS was used to deconvolute the core-level spectra. The relative contribution of the 1T and 2H phase to the Mo⁴⁺ 3d_{3/2} and Mo⁴⁺ 3d_{5/2} was used to calculate the 2H content, as described by Papageorgopoulos *et al.*^{8,36} Meanwhile, a SpectraMax M2Microplate Reader with a cuvette port was used for UV-vis spectroscopy to estimate the 1T/2H ratio of the MoS₂ nanosheets. The 2H content of MoS₂ can be estimated using an empirical relation derived by Knirsch *et al.*³⁹ E_{410} and E_{350} , which represent the absorbance at 410 and 350 nm, respectively, were used in the following equation to calculate the 2H ra-

ratio: $\frac{2H}{1T+2H} = 1.29 - 2.562 \times 0.287 \frac{E_{410}}{E_{350}}$. The absorbance obtained at 350 nm is associated with strong 1T contribution, while the absorbance at 410 nm is related to strong 2H contribution.³⁹

Preparation of Monolayer Electrodes. Prior to preparation of the deposited dispersion, the nanosheet suspensions in DMF were sonicated for 10 min. Then, the nanosheet suspensions were diluted

with equal parts DMF and 1,2-dichloroethane (DCE) until concentrations of 0.055 and 0.00625 mg/mL were achieved for the MoS₂ and rGO nanosheet suspensions, respectively. Fairly dilute nanosheet dispersions and a water immiscible, volatile spreading solvent such as DCE are required for successful deposition.⁶ Aggregates were removed by centrifugation in 15 mL glass tubes at 4000 rpm for 1 h prior to deposition.

Monolayer films were deposited onto the air/water interface of a polytetrafluoroethylene (PTFE) trough, as shown in Figure 1a. The total available water surface area (15.8 cm × 12.7 cm) for film formation was approximately 200 cm². The trough was first cleaned by rinsing with deionized water and wiped with DCE. Dispersions were then added to the air–water surface *via* a syringe pump (KD Scientific) using a glass syringe equipped with PTFE tubing (0.312 mm outer diameter) at a flow rate of 0.13 mL/min. The end of the tubing was positioned such that the droplet formed was just above the air/water interface. Too high of a position can lead to penetration of the drop through the air/water interface and into the bulk instead of spreading on the surface, as is required for successful transfer. Deposition was carried out until approximately 20% of the ~200 cm² water surface remained uncovered by the film of densely tiled nanosheets.

The horizontal precipitation method^{5,6,23,27} was used to deposit the floating films of rGO or MoS₂ onto various clean substrates placed under the water prior to deposition. These included freshly cleaved mica and HOPG as well as clean glass slides and SiO₂ wafers. Double- and triple-layer films were fabricated by repeated deposition on already coated substrates after drying the substrates for 1 min on a hot plate at 60 °C. To restore the 2H phase of the MoS₂ films, 1T MoS₂ electrodes were heat treated at 300 °C, according to a process reported by Acerce *et al.*⁷ Electrodes were placed in a quartz tube which was purged and filled with Ar (99.999%) three times. Then, the electrodes were annealed at 300 °C in a furnace (Lindburg Blue M) under argon with a 10 sccm flow for 1 h. Additional samples were annealed at 150 °C to obtain an intermediate 2H content.

Characterization of Monolayer Electrodes. Single-, double-, and triple-layer rGO and MoS₂ films were characterized using UV–vis spectroscopy to determine the transmittance on glass substrates. Atomic force microscope (AFM) images were taken using a Digital Instruments Nanoscope IV to determine flake size, roughness, and film coverage using contact mode and Bruker, NP-STM10 tips. These images were assessed using Gwyddion software to determine surface roughness, by dividing the projected area of the sample by the measured surface area. A Python script was also used to determine fractional coverage and average sheet thickness. This script fit the raw height data of the image to a sum of Gaussian curves representing sheets of various average thickness. Film coverage was also observed by scanning electron microscopy (SEM) using a field emission scanning electron microscope (LEO 1550, Zeiss) with an acceleration voltage of 10 kV. These SEM images were analyzed using ImageJ.

The electrodes were characterized using a custom-made 3D-printed polypropylene electrochemical cell mimicking the same design previously reported that used machined PTFE.^{23,27} In this configuration, the exposed surface area of the electrodes was controlled *via* spring-loading against an O-ring, as shown in Figure 1b.

For testing in aqueous electrolyte, 1 M NaF dissolved in ultrahigh-purity Milli-Q water was used as the electrolyte. This was used in an attempt to eliminate specific adsorption, as NaF is relatively nonadsorbing and often used in fundamental studies of double-layer charging.^{24,28,29} A Ag/AgCl reference electrode (1 M) and Pt wire counter electrode (0.5 mm diameter, 99.99% purity) were used. For testing in organic electrolyte, the cell was filled with 0.1 M tetrafluoroborate (TEABF₄) in acetonitrile (AN), and two Pt wires were used as a quasi-reference and counter electrode. One mM ferrocene was added to the electrolyte immediately after the measurement to define the reference potential using cyclic voltammetry (CV). Perfluoroelastomer O-rings were employed to minimize swelling in organic electrolytes.

CV and electrochemical impedance spectroscopy (EIS) were performed with a SP-300 potentiostat (Bio-Logic USA). Samples

were tested in a voltage window of -0.3 to 0.5 V. This voltage window was chosen because apparent faradaic reactions would occur at voltages greater than 0.5 V and less than -0.3 V. Potential dependence was typically plotted at 100 Hz in an attempt to eliminate slower Faradaic charging processes from the measurement, while frequency dependence was plotted at -0.14 V *vs* Ag/AgCl (1 M), the approximate OCV of all coated samples.

Capacitance values were calculated from CV measurements using eq 2:

$$C = \frac{\int IdV}{v \times A \times \Delta V} \quad (2)$$

where $\int IdV$ is the area under the CV curve, v is the scan rate (100 mV/s), A is the exposed area of the electrochemical cell, and ΔV is the potential stability window (0.8 V). However, since calculations made with EIS measurements only examined values at the open circuit potential (approximately -0.14 V), a second calculation was made using eq 3:

$$C = \frac{\Delta I_{\text{OCV}} \Delta V}{v \times A \times \Delta V} = \frac{I_{\text{OCV}}}{v \times A} \quad (3)$$

where ΔI_{OCV} is the difference in current values recorded at the open circuit potential. These values are denoted as CV@OCV.

ASSOCIATED CONTENT

Supporting Information

The Supporting Information is available free of charge at <https://pubs.acs.org/doi/10.1021/acsnano.9b10182>.

Further information on additional experimental details, explanation of image analysis methods, further analysis of Langmuir film formation, materials characterization and electrochemical analysis graphs ([PDF](#))

AUTHOR INFORMATION

Corresponding Author

Michael A. Pope – Department of Chemical Engineering,
University of Waterloo, Waterloo, Ontario N2L 3G1, Canada;
orcid.org/0000-0002-5793-3392; Email: michael.pope@uwaterloo.ca

Authors

Jialu Chen – Department of Chemical Engineering, University of Waterloo, Waterloo, Ontario N2L 3G1, Canada
Wesley R. Walker – Department of Chemical Engineering, University of Waterloo, Waterloo, Ontario N2L 3G1, Canada
Luzhu Xu – Department of Chemical Engineering, University of Waterloo, Waterloo, Ontario N2L 3G1, Canada
Olga Krysiak – Department of Chemical Engineering, University of Waterloo, Waterloo, Ontario N2L 3G1, Canada
Zimin She – Department of Chemical Engineering, University of Waterloo, Waterloo, Ontario N2L 3G1, Canada

Complete contact information is available at:
<https://pubs.acs.org/10.1021/acsnano.9b10182>

Notes

The authors declare no competing financial interest.

ACKNOWLEDGMENTS

J.C. would like to acknowledge funding support from the Ontario Graduate Scholarship (OGS) and the Waterloo Institute for Nanotechnology (WIN) Nanofellowship program. W.R.W., L.X., and M.A.P. acknowledge support from the Natural Sciences and Engineering Research Council of Canada

(NSERC) Discovery Grant program. Z.S. acknowledges support from the China Scholarship Council.

REFERENCES

- Kumar, K. S.; Choudhary, N.; Jung, Y.; Thomas, J. Recent Advances in Two-Dimensional Nanomaterials for Supercapacitor Electrode Applications. *ACS Energy Lett.* **2018**, *3*, 482–495.
- Theerthagiri, J.; Senthil, R. A.; Senthilkumar, B.; Reddy Polu, A.; Madhavan, J.; Ashokkumar, M. Recent Advances in MoS₂ Nanostructured Materials for Energy and Environmental Applications - A Review. *J. Solid State Chem.* **2017**, *252*, 43–71.
- Rao, C. N. R.; Gopalakrishnan, K.; Maitra, U. Comparative Study of Potential Applications of Graphene, MoS₂, and Other Two-Dimensional Materials in Energy Devices, Sensors, and Related Areas. *ACS Appl. Mater. Interfaces* **2015**, *7*, 7809–7832.
- Conway, B. E. *Electrochemical Supercapacitors: Scientific Fundamentals and Technological Applications*; Kluwer Academic and Plenum: New York, 1999; Vol. 1.
- Xu, L.; Tetreault, A. R.; Khaligh, H. H.; Goldthorpe, I. A.; Wettig, S. D.; Pope, M. A. Continuous Langmuir-Blodgett Deposition and Transfer by Controlled Edge-to-Edge Assembly of Floating 2D Materials. *Langmuir* **2019**, *35*, 51–59.
- Zhang, Y.; Xu, L.; Walker, W. R.; Tittle, C. M.; Backhouse, C. J.; Pope, M. A. Langmuir Films and Uniform, Large Area, Transparent Coatings of Chemically Exfoliated MoS₂ Single Layers. *J. Mater. Chem. C* **2017**, *5*, 11275–11287.
- Acerce, M.; Voiry, D.; Chhowalla, M. Metallic 1T Phase MoS₂ Nanosheets as Supercapacitor Electrode Materials. *Nat. Nanotechnol.* **2015**, *10*, 313–318.
- Voiry, D.; Mohite, A.; Chhowalla, M. Phase Engineering of Transition Metal Dichalcogenides. *Chem. Soc. Rev.* **2015**, *44*, 2702–2712.
- Wypych, F.; Schöllhorn, R. 1T-MoS₂, a New Metallic Modification of Molybdenum Disulfide. *J. Chem. Soc., Chem. Commun.* **1992**, No. 19, 1386–1388.
- Eda, G.; Yamaguchi, H.; Voiry, D.; Fujita, T.; Chen, M.; Chhowalla, M. Photoluminescence from Chemically Exfoliated MoS₂. *Nano Lett.* **2011**, *11*, 5111–5116.
- Sim, D. M.; Han, H. J.; Yim, S.; Choi, M. J.; Jeon, J.; Jung, Y. S. Long-Term Stable 2H-MoS₂ Dispersion: Critical Role of Solvent for Simultaneous Phase Restoration and Surface Functionalization of Liquid-Exfoliated MoS₂. *ACS Omega* **2017**, *2*, 4678–4687.
- Acerce, M.; Voiry, D.; Chhowalla, M. Metallic 1T Phase MoS₂ Nanosheets as Supercapacitor Electrode Materials. *Nat. Nanotechnol.* **2015**, *10*, 313–318.
- Wu, J.; Dai, J.; Shao, Y.; Cao, M.; Wu, X. Carbon Dot-Assisted Hydrothermal Synthesis of Flower-Like MoS₂ Nanospheres Constructed by Few-Layered Multiphase MoS₂ Nanosheets for Supercapacitors. *RSC Adv.* **2016**, *6*, 77999–78007.
- Fang, L.; Qiu, Y.; Li, W.; Wang, F.; Lan, M.; Huang, K.; Jing, Q. Three-Dimensional Flower-Like MoS₂-CoSe₂ Heterostructure for High Performance Supercapacitors. *J. Colloid Interface Sci.* **2018**, *512*, 282–290.
- Lingappan, N.; Van, N. H.; Lee, S.; Kang, D. J. Growth of Three Dimensional Flower-Like Molybdenum Disulfide Hierarchical Structures on Graphene/Carbon Nanotube Network: An Advanced Heterostructure for Energy Storage Devices. *J. Power Sources* **2015**, *280*, 39–46.
- Chen, M.; Wang, J.; Yan, X.; Ren, J.; Dai, Y.; Wang, Q.; Wang, Y.; Cheng, X. Flower-Like Molybdenum Disulfide Nanosheets Grown on Carbon Nanosheets to Form Nanocomposites: Novel Structure and Excellent Electrochemical Performance. *J. Alloys Compd.* **2017**, *722*, 250–258.
- Ilanchezhian, P.; Mohan Kumar, G.; Kang, T. W. Electrochemical Studies of Spherically Clustered MoS₂ Nanostructures for Electrode Applications. *J. Alloys Compd.* **2015**, *634*, 104–108.
- Lin, T. W.; Hsiao, M. C.; Wang, A. Y.; Lin, J. Y. Hollow Hierarchical Carbon Spheres Decorated with Ultrathin Molybdenum

- Disulfide Nanosheets as High-Capacity Electrode Materials for Asymmetric Supercapacitors. *ChemElectroChem* **2017**, *4*, 620–627.
- (19) Kamila, S.; Mohanty, B.; Samantara, A. K.; Guha, P.; Ghosh, A.; Jena, B.; Satyam, P. V.; Mishra, B. K.; Jena, B. K. Highly Active 2D Layered MoS₂-RGO Hybrids for Energy Conversion and Storage Applications. *Sci. Rep.* **2017**, *7*, 8378.
- (20) Nandi, D. K.; Sahoo, S.; Sinha, S.; Yeo, S.; Kim, H.; Bulakhe, R. N.; Heo, J.; Shim, J. J.; Kim, S. H. Highly Uniform Atomic Layer-Deposited MoS₂@3D-Ni-Foam: A Novel Approach to Prepare an Electrode for Supercapacitors. *ACS Appl. Mater. Interfaces* **2017**, *9*, 40252–40264.
- (21) Balasingam, S. K.; Lee, M.; Kim, B. H.; Lee, J. S.; Jun, Y. Freeze-Dried MoS₂ Sponge Electrodes for Enhanced Electrochemical Energy Storage. *Dalt. Trans.* **2017**, *46*, 2122–2128.
- (22) She, Z.; Ghosh, D.; Pope, M. A. Decorating Graphene Oxide with Ionic Liquid Nanodroplets: An Approach Leading to Energy-Dense, High-Voltage Supercapacitors. *ACS Nano* **2017**, *11*, 10077–10087.
- (23) Pope, M. A.; Punckt, C.; Aksay, I. A. Intrinsic Capacitance and Redox Activity of Functionalized Graphene Sheets. *J. Phys. Chem. C* **2011**, *115*, 20326–20334.
- (24) Xia, J.; Chen, F.; Li, J.; Tao, N. Measurement of the Quantum Capacitance of Graphene. *Nat. Nanotechnol.* **2009**, *4*, 505–509.
- (25) Fang, T.; Konar, A.; Xing, H.; Jena, D. Carrier Statistics and Quantum Capacitance of Graphene Sheets and Ribbons. *Appl. Phys. Lett.* **2007**, *91*, 092109.
- (26) Stoller, M. D.; Magnuson, C. W.; Zhu, Y.; Murali, S.; Suk, J. W.; Piner, R.; Ruoff, R. S. Interfacial Capacitance of Single Layer Graphene. *Energy Environ. Sci.* **2011**, *4*, 4685–4689.
- (27) Pope, M. A.; Aksay, I. A. Four-Fold Increase in the Intrinsic Capacitance of Graphene through Functionalization and Lattice Disorder. *J. Phys. Chem. C* **2015**, *119*, 20369–20378.
- (28) Randin, J.-P.; Yeager, E. Differential Capacitance Study on the Basal Plane of Stress-Annealed Pyrolytic Graphite. *J. Electroanal. Chem. Interfacial Electrochem.* **1972**, *36*, 257.
- (29) Randin, J.-P.; Yeager, E. Differential Capacitance Study on the Edge Orientation of Pyrolytic Graphite and Glassy Carbon Electrodes. *J. Electroanal. Chem. Interfacial Electrochem.* **1975**, *58*, 313–322.
- (30) Gerischer, H. An Interpretation of the Double Layer Capacity of Graphite Electrodes in Relation to the Density of States at the Fermi Level. *J. Phys. Chem.* **1985**, *89*, 4249–4251.
- (31) Goh, M. S.; Pumera, M. Multilayer Graphene Nanoribbons Exhibit Larger Capacitance than Their Few-Layer and Single-Layer Graphene Counterparts. *Electrochim. Commun.* **2010**, *12*, 1375–1377.
- (32) Paek, E.; Pak, A. J.; Hwang, G. S. A Computational Study of the Interfacial Structure and Capacitance of Graphene in [BMIM][PF₆] Ionic Liquid. *J. Electrochem. Soc.* **2013**, *160*, A1–A10.
- (33) Helmholtz, H. Studien Über Electriche Grenzschichten. *Ann. Phys.* **1879**, *243*, 337–382.
- (34) Kerisit, S.; Schwenzer, B.; Vijayakumar, M. Effects of Oxygen-Containing Functional Groups on Supercapacitor Performance. *J. Phys. Chem. Lett.* **2014**, *5*, 2330–2334.
- (35) Liu, Z.; Jiang, L.; Sheng, L.; Zhou, Q.; Wei, T.; Zhang, B.; Fan, Z. Oxygen Clusters Distributed in Graphene with “Paddy Land” Structure: Ultrahigh Capacitance and Rate Performance for Supercapacitors. *Adv. Funct. Mater.* **2018**, *28*, 1705258.
- (36) Papageorgopoulos, C. A.; Jaegermann, W. Li Intercalation across and along the van der Waals Surfaces of MoS₂ (0001). *Surf. Sci.* **1995**, *338*, 83–93.
- (37) Xu, L.; Tetreault, A. R.; Pope, M. A. Chemical Insights into the Rapid, Light-Induced Auto-Oxidation of Molybdenum Disulfide Aqueous Dispersions. *Chem. Mater.* **2020**, *32*, 148–156.
- (38) Chacko, L.; Rastogi, P. K.; Aneesh, P. M. Phase Engineering from 2H to 1T-MoS₂ for Efficient Ammonia PL Sensor and Electrocatalyst for Hydrogen Evolution Reaction. *J. Electrochem. Soc.* **2019**, *166*, H263–H271.
- (39) Knirsch, K. C.; Berner, N. C.; Nerl, H. C.; Cucinotta, C. S.; Gholamvand, Z.; McEvoy, N.; Wang, Z.; Abramovic, I.; Vecera, P.; Halik, M.; Sanvito, S.; Duesberg, G. S.; Nicolosi, V.; Hauke, F.; Hirsch, A.; Coleman, J. N.; Backes, C. Basal-Plane Functionalization of Chemically Exfoliated Molybdenum Disulfide by Diazonium Salts. *ACS Nano* **2015**, *9*, 6018–6030.
- (40) Attanayake, N. H.; Thenuwara, A. C.; Patra, A.; Aulin, Y. V.; Tran, T. M.; Chakraborty, H.; Borguet, E.; Klein, M. L.; Perdew, J. P.; Strongin, D. R. Effect of Intercalated Metals on the Electrocatalytic Activity of 1T-MoS₂ for the Hydrogen Evolution Reaction. *ACS Energy Lett.* **2018**, *3*, 7–13.
- (41) Lembke, D.; Kis, A. Breakdown of High-Performance Monolayer MoS₂ Transistors. *ACS Nano* **2012**, *6*, 10070–10075.
- (42) Nair, R. R.; Blake, P.; Grigorenko, A. N.; Novoselov, K. S.; Booth, T. J.; Stauber, T.; Peres, N. M. R.; Geim, A. K. Fine Structure Constant Defines Visual Transparency of Graphene. *Science (Washington, DC, U. S.)* **2008**, *320*, 1308–1308.
- (43) Qu, D.; Shi, H. Studies of Activated Carbons Used in Double-Layer Capacitors. *J. Power Sources* **1998**, *74*, 99–107.
- (44) Aldama, I.; Barranco, V.; Kunowsky, M.; Ibañez, J.; Rojo, J. M. Contribution of Cations and Anions of Aqueous Electrolytes to the Charge Stored at the Electric Electrolyte/Electrode Interface of Carbon-Based Supercapacitors. *J. Phys. Chem. C* **2017**, *121*, 12053–12062.
- (45) Kemp, D. D.; Gordon, M. S. Theoretical Study of the Solvation of Fluorine and Chlorine Anions by Water. *J. Phys. Chem. A* **2005**, *109*, 7688–7699.
- (46) Mamardashvili, G. M.; Mamardashvili, N. Z.; Koifman, O. I. Synthesis and Receptor Properties of Calix[4]Pyrroles. *Russ. Chem. Rev.* **2015**, *84*, 275–287.
- (47) Nightingale, E. R. Phenomenological Theory of Ion Solvation. Effective Radii of Hydrated Ions. *J. Phys. Chem.* **1959**, *63*, 1381–1387.
- (48) Marcus, Y. A Simple Empirical Model Describing the Thermodynamics of Hydration of Ions of Widely Varying Charges, Sizes, and Shapes. *Biophys. Chem.* **1994**, *51*, 111–127.
- (49) Sun, T.; Li, Z.; Liu, X.; Ma, L.; Wang, J.; Yang, S. Oxygen-Incorporated MoS₂ Microspheres with Tunable Interiors as Novel Electrode Materials for Supercapacitors. *J. Power Sources* **2017**, *352*, 135–142.
- (50) Zhou, J.; Fang, G.; Pan, A.; Liang, S. Oxygen-Incorporated MoS₂ Nanosheets with Expanded Interlayers for Hydrogen Evolution Reaction and Pseudocapacitor Applications. *ACS Appl. Mater. Interfaces* **2016**, *8*, 33681–33689.
- (51) Anand, H.; Verma, R. Solvation of Some Tetraalkylammonium Salts Investigated Conductometrically and Viscometrically in Binary Mixtures of Acetonitrile + Methanol at 298.15 K. *Z. Phys. Chem.* **2016**, *230*, 1759–1772.
- (52) Davelou, D.; Kopidakis, G.; Kiouseoglou, G.; Remediakis, I. N. MoS₂ Nanostructures: Semiconductors with Metallic Edges. *Solid State Commun.* **2014**, *192*, 42–46.
- (53) Gerischer, H. *Advances in Electrochemistry and Electrochemical Engineering*; Interscience Publishers: Geneva, Switzerland, 1961; Vol. 1, p 155.
- (54) Lee, S. K.; Chu, D.; Song, D. Y.; Pak, S. W.; Kim, E. K. Electrical and Photovoltaic Properties of Residue-Free MoS₂ Thin Films by Liquid Exfoliation Method. *Nanotechnology* **2017**, *28*, 195703.
- (55) Wang, K. C.; Staney, T. K.; Valencia, D.; Charles, J.; Henning, A.; Sangwan, V. K.; Lahiri, A.; Mejia, D.; Sarangapani, P.; Povolotskyi, M.; Afzalian, A.; Maassen, J.; Klimeck, G.; Hersam, M. C.; Lauhon, L. J.; Stern, N. P.; Kubis, T. Control of Interlayer Physics in 2H Transition Metal Dichalcogenides. *J. Appl. Phys.* **2017**, *122*, 224302.
- (56) Hou, Y.; Aoki, K. J.; Chen, J.; Nishiumi, T. Solvent Variables Controlling Electric Double Layer Capacitance at the Metal-Solution Interface. *J. Phys. Chem. C* **2014**, *118*, 10153–10158.
- (57) Worsley, M. A.; Shin, S. J.; Merrill, M. D.; Lenhardt, J.; Nelson, A. J.; Woo, L. Y.; Gash, A. E.; Baumann, T. F.; Orme, C. A. Ultralow Density, Monolithic WS₂, MoS₂, and MoS₂/Graphene Aerogels. *ACS Nano* **2015**, *9*, 4698–4705.
- (58) Zhang, T.; Kong, L.-B.; Liu, M.-C.; Dai, Y.-H.; Yan, K.; Hu, B.; Luo, Y.-C.; Kang, L. Design and Preparation of MoO₂/MoS₂ as

Negative Electrode Materials for Supercapacitors. *Mater. Des.* **2016**, *112*, 88–96.

(59) Hummers, W. S.; Offeman, R. E. Preparation of Graphitic Oxide. *J. Am. Chem. Soc.* **1958**, *80*, 1339.

(60) Marcano, D. C.; Kosynkin, D. V.; Berlin, J. M.; Sinitskii, A.; Sun, Z.; Slesarev, A.; Alemany, L. B.; Lu, W.; Tour, J. M. Improved Synthesis of Graphene Oxide. *ACS Nano* **2010**, *4*, 4806–4814.

(61) Park, S.; An, J.; Jung, I.; Piner, R. D.; An, S. J.; Li, X.; Velamakanni, A.; Ruoff, R. S. Colloidal Suspensions of Highly Reduced Graphene Oxide in a Wide Variety of Organic Solvents. *Nano Lett.* **2009**, *9*, 1593–1597.